ACS MATERIALS LETTERS

www.acsmaterialsletters.org

Combined Effect of Fluoride Enables the Stable Charging−Discharging Cycle of Carbonate-Based Li-Ion Pouch Cells at −30 °C

Hao Huang, Yiyang Zhao, Jingang Zheng, Weichen Han, Hongxu Zhou, Hongyang Li, Hongquan Chai, Lixiang Li, Hongwei Zhao, Han Zhang, Baigang An,* and Chengguo Sun*

Cite This: *ACS Materials Lett.* 2025, 7, 1321−1328

Read Online

ACCESS | Metrics & More | Article Recommendations | Supporting Information

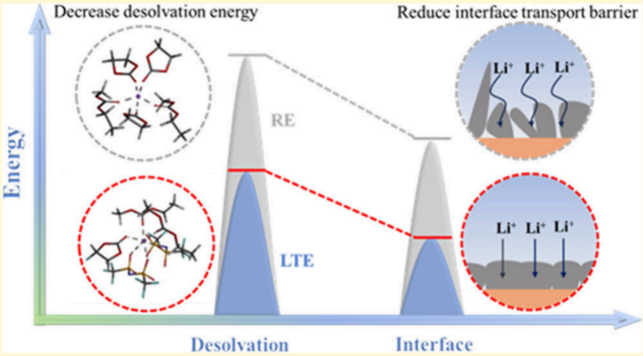

ABSTRACT: **Carbonate-based electrolytes in Li-ion batteries are limited by low-temperature performance due to their slow ion transport kinetics and high interfacial transport energy barriers. Herein, we propose a component modulation strategy from the combined effect of fluor-solvents and fluor-additives, where the noncoordinated 1,1,2,2-tetrafluoroethyl-2,2,3,3-tetrafluoropropylether was introduced into a 2.0 M lithium bis(trifluoromethanesulfonyl)imide, fluoroethylene carbonate, and ethyl methyl carbonate electrolyte to promote more cation−anion coordination, thus decreasing Li-ion desolvation energy. Subsequently, the additives of lithium difluoro(oxalato)borate, lithium difluorophosphate, and ethylene sulfate were adopted to construct robust interface layers with inorganic components, reducing the interface transport barrier of the Li-ion. As result, the Li‖NCM811 cells achieve an average capacity of 132.2 mAh g^{-1} at 0.2 C and −30 °C during the 100 charge−discharge cycles. Significantly, the graphite‖NCM523 pouch cell delivers a high initial discharge capacity of 0.85 Ah at −30 °C and 88% capacity retention after 200 charge−discharge cycles.**

Ethylene carbonate (EC)-based electrolytes have contributed to the development of Li-ion batteries (LIBs) for their high ionic conductivity and superior compatibility with graphite anode.[1−3] However, the strong interaction of Li$^+$-solvents and organic-rich solid electrolyte interphase in EC-based electrolyte result in the suppressed Li-ion transport and high interfacial transfer energy barrier at low temperature.[4,5] Thus, regulating the solvation structure and interfacial layer structure with fast ion transport is the key to achieving low-temperature operation.

Massive strategies have been proposed to address the issues including film-forming additive,[6] low concentration electrolyte,[7] the weak solvating electrolyte,[8,9] local high-concentration electrolyte,[10−14] all fluorinated carbonate-based electrolyte,[15,16] dual-lithium salt electrolyte,[17] ion liquid electrolyte,[18,19] and novel ether and carboxylic acid ester electrolyte.[20−24] For example, all fluorinated carbonate-based electrolytes enable Li‖NCM811 coin cells to display a discharge capacity of 143.5 mAh g^{-1} for 5 cycles at −30 °C and 0.1 C.[15] The weak solvating electrolyte with noncoordinated diluent can facilitate the formation of TFSI$^-$-derived SEI, allowing the Li‖LFP pouch cell to cycle at 0.1 C for 5 cycles, 0.2 C for 5 cycles, and 0.3 C for 14 cycles at −20 °C.[9] Employing 1 mol L^{-1} LiTFSI in MDFA/MDFSA/TTE electrolyte to obtain a single-layer NCM811‖graphite pouch cell can maintain 80% capacity retention after 360th cycle at −30 °C and 0.2 C.[20] Moreover, the lithium hexafluorophosphate (LiPF$_6$)-based local high-concentration electrolyte with lithium difluorobis(oxalato)-phosphate is designed to enhance the performance of LIBs, the graphite‖NCM622 pouch cell delivers a capacity of 106 mAh g^{-1} at −20 °C and 0.1 C.[13] Although this progress has made significant contributions to the low-temperature performance of LIBs, the long cycling stability and stable charge−discharge cycles of Li-ion pouch cell with carbonate-based electrolyte at low temperature (≤−20 °C) are still urgently needed. Especially, reasonable construction of electrolyte formulating

Received: January 18, 2025
Revised: March 6, 2025
Accepted: March 7, 2025
Published: March 12, 2025

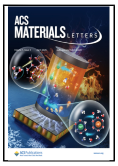

https://doi.org/10.1021/acsmaterialslett.5c00130

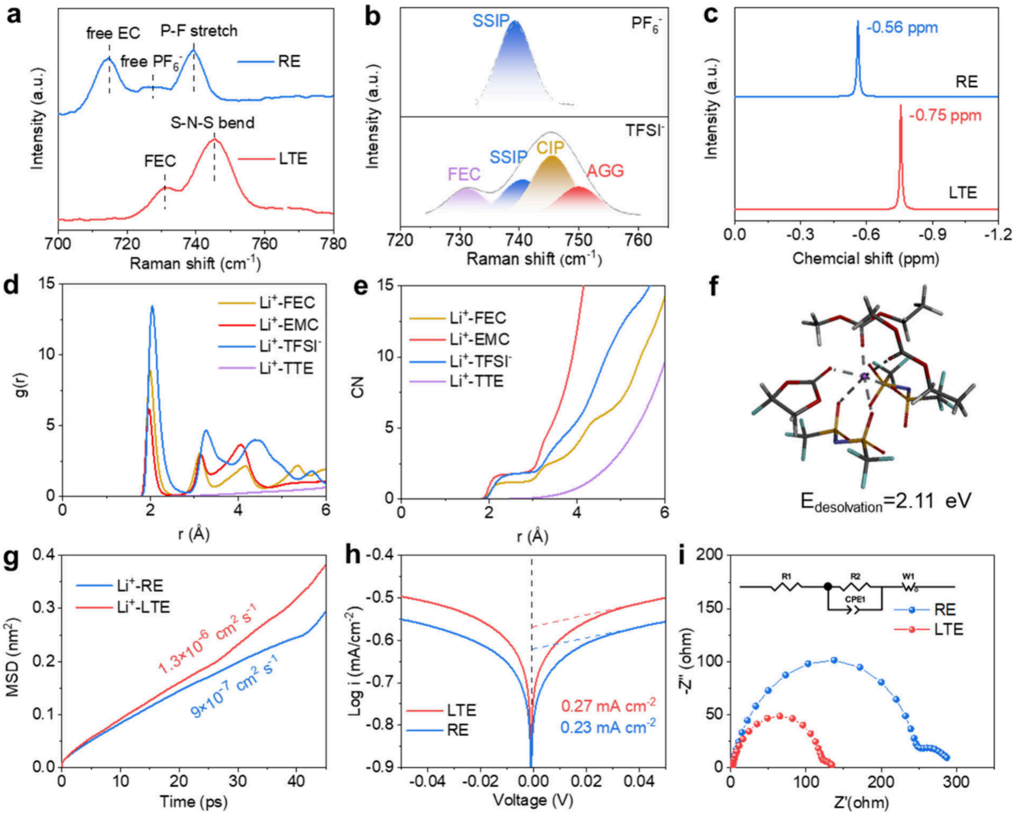

Figure 1. (a) Raman spectra of RE and LTE. (b) The vibration band of $TFSI^-$ and PF_6^- in the range 720−765 cm^{-1}. (c) ^7Li NMR spectra of RE and LTE. (d) The radial distribution function of Li-ion in LTE. (e) Coordination number plots of Li-ion in LTE. (f) The typical solvation structure of LTE. (g) Mean square displacement curves and diffusion coefficient of Li-ion in RE and LTE. (h) Tafel plots of Li||Li cells in different electrolytes. (i) EIS curves of Li||Li cells in different electrolytes.

ingredients for LIBs with a long lifespan at low temperature should be capable of rapid desolvation and formation of a tough inorganic-rich interface layer.[25−27]

In this work, a noncoordinated 1,1,2,2-tetrafluoroethyl-2,2,3,3-tetrafluoropropylether (TTE) was introduced to a 2.0 M lithium bis(trifluoromethanesulfonyl)imide (LiTFSI), fluoroethylene carbonate (FEC) and ethyl methyl carbonate (EMC) electrolyte electrolyte for promoting more cation−anion coordination, the Li^+-solvent-$TFSI^-$ structure can decrease Li-ion desolvation energy. Meanwhile, lithium difluoro(oxalato)borate (LiDFOB), lithium difluorophosphate ($LiPO_2F_2$), and ethylene sulfate (DTD) were added to in situ form robust interface layers with inorganic components, reducing the interface transport barrier of the Li-ion. Application of the designed electrolyte in Li||NCM811 cells can achieve 80% capacity retention after 500 cycles at 25 °C and 99% capacity retention at −30 °C after 100 cycles. The practical graphite||NCM523 pouch cells enable high initial discharge capacity of 0.85 Ah at −30 °C, and 88% capacity retention after 200 cycles. This study offers a framework for enhancing low temperature performance and cycling stability in alkali-metal-ion batteries.

The low temperature electrolyte (LTE) is prepared by introducing equal volume TTE and 0.5 wt % LiDFOB, 0.5 wt % $LiPO_2F_2$ and 1 wt % DTD to 2.0 M LiTFSI-FEC/EMC (3/7, by volume) electrolyte. Commercial electrolyte (1 M $LiPF_6$ and 2 wt % LiDFOB in EC/EMC with volume ratio of 3/7) serves as reference electrolyte (RE). The physical properties of RE and LTE electrolyte are summarized in Figures S1−S4 and Table S1, it is worth mentioning that the ion conductivity and Li^+ transference number of LTE are as high as 1.07 mS cm^{-1} at −25 °C and 0.75 at 20 °C, respectively. Figure 1a shows the Raman spectra of RE and LTE electrolyte within the range of 700−780 cm^{-1}, the RE contains the peaks of free EC, free PF_6^-, and P−F stretch vibration, and the PF_6^- mainly exists in the form of solvent-separated ion pairs (SSIPs). In contrast, there are only two peaks of free FEC and S−N−S bend vibration in LTE. The vibration band of $TFSI^-$ includes three modes: SSIPs, contact ion pairs (CIPs), and ion aggregates (AGGs).[28−30] It is worth mentioning that the $TFSI^-$ anion recruited into the Li-ion solvation sheath, with the ratio of CIP and AGG as high as 75%. Figure 1c shows ^7Li nuclear magnetic resonance spectra of RE and LTE, the chemical shift of RE and LTE is −0.56 and −0.75 ppm, suggesting a stronger solvation effect between Li^+ and anion than that of RE.[31,32] To further investigate the coordination of Li-ion, molecular dynamics simulation results of cell A (LTE) and cell B (RE) are presented in Figure S5, indicating that introduction of TTE and increase of the concentration of LiTFSI can promote anion aggregation. In the LTE, the Li^+ are primarily coordinated by 1.33 FEC, 2.25 EMC, and 1.90 TFSI-, the corresponding peak of Li−O at 1.99, 1.96, and 2.05 Å, all located in the first solvation sheath of Li-ion (<3 Å). In contrast, the Li-ion is chiefly surrounded by the solvent molecules in RE, and there are 2.71 EC and 2.72 EMC coordinated with the Li-ion (Figure S6). Significantly, the typical solvation structures of LTE and RE are shown in Figure 1f and Figure S7, respectively. The desolvation energy of LTE is 2.11 eV, which is much smaller than that of RE (5.49 and 6.20 eV). Figure 1g shows the mean squared displacement of

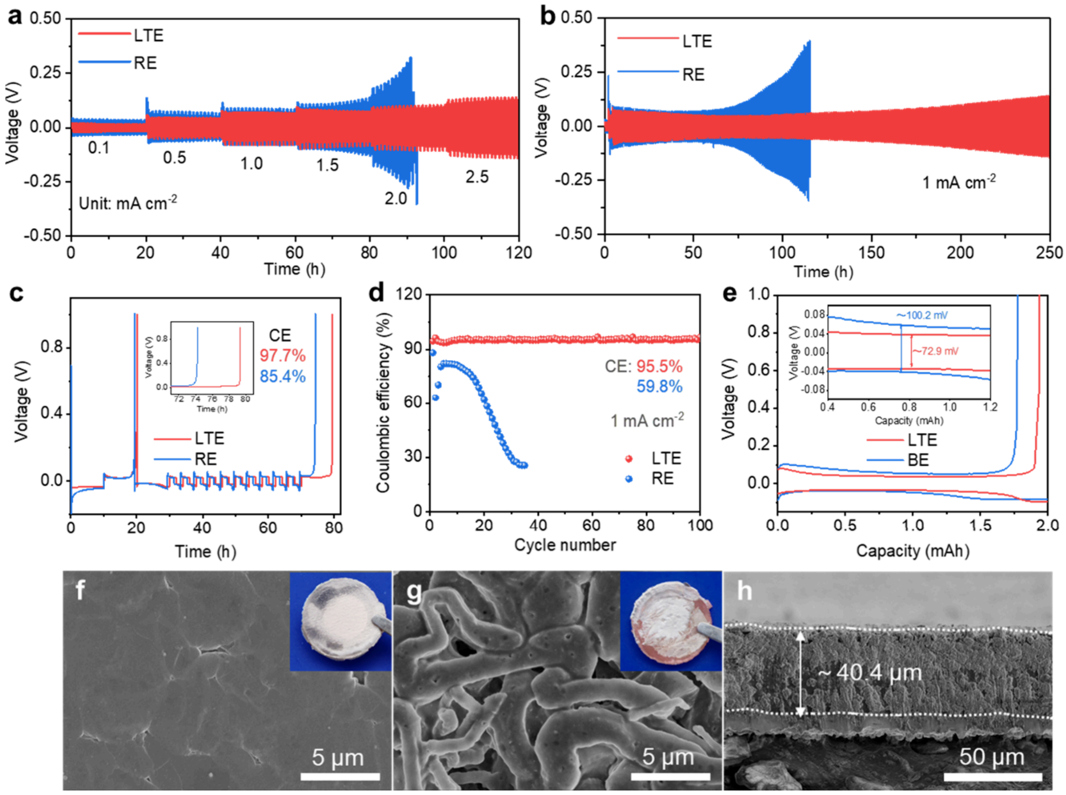

Figure 2. (a) Rate performances of symmetrical Li||LTE||Li and Li||RE||Li at 25 °C. (b) Cycling performance of Li||LTE||Li and Li||RE||Li at 25 °C and 1 mA cm^{-2}. (c) Aurbach test of Li||LTE||Cu and Li||RE||Cu cells. (d) Cycling performance of Li||LTE||Cu and Li||RE||Cu cells at 1 mA cm^{-2}. (e) Charge−discharge voltage profiles of Li||LTE||Cu and Li||RE||Cu cells at the 20th cycle. (f) SEM image of the electrodeposited lithium at 10 mAh on the Cu foils in LTE, the corresponding optical image is inserted in the upper right corner. (g) SEM image of the electrodeposited lithium at 10 mAh on the Cu foils in RE, the corresponding optical image is inserted in the upper right corner. (h) The cross-section SEM image of the electrodeposited lithium at 10 mAh on the Cu foils in LTE.

different electrolytes; the Li-ion diffusivity of LTE was calculated to be 1.3 × 10^{-6} cm^2 s^{-1}, which is 1.44 times as high as RE (9 × 10^{-7} cm^2 s^{-1}). In addition, the exchange current density extracted from Li||LTE||Li cell (0.27 mA cm^{-2}) is higher than that of Li||RE||Li cell (0.23 mA cm^{-2}), which further demonstrates facile Li-ion transport in LTE electrolyte.[33,34] Figure 1i shows that the resistance value of Li||LTE||Li is 122.32 Ω, which was much smaller than that of Li||RE||Li cell (249.28 Ω). The above results demonstrate that LTE facilitates rapid Li-ion desolvation and interface transportation, which is expected to achieve a high capacity under extreme cold operating conditions.

The interface compatibility between the electrolyte and Li metal anode is necessary for electrolyte applicability. Figure 2a shows the delivered voltage hysteresis values of Li-symmetric cells with the LTE and RE electrolytes. After increasing the current density from 0.1 to 0.5, 1.0, 1.5, 2.0, and 2.5 mA cm^{-2}, the Li-symmetric cells employing LTE exhibited voltage hysteresis values of 21, 49, 73, 80, 100, and 140 mV, respectively. However, Li||RE||Li exhibits higher voltage hysteresis values of 41, 74, 90, 120, and 210 mV at 0.1, 0.5, 1, 1.5, and 2 mA cm^{-2}, respectively. It is worth mentioning that the polarization voltage rapidly increases at 2 mA cm^{-2}, and the Li||RE||Li cells ultimately fail. At a lower current density of 1 mA cm^{-2}, the Li||RE||Li cells still display high voltage polarization and rapid voltage increase, lasting only 115 h of cycling. In contrast, the Li||LTE||Li cells show a slow voltage growth and achieve at least 250 h of long-term cycle life (Figure 2b and Figure S8), and the Li||LTE||Li cells also achieve at least 80 h of cycle life at −30 °C. (Figure S9) To further prove the high compatibility of LTE with metallic Li, the average Coulombic efficiency (CE$_{avg}$) during the Li depositing/striping was calculated by harsh Li−Cu cells Aurbach test, the calculated CE$_{avg}$ of LTE and RE are 97.7% and 85.4%, respectively (Figure 2c). As expected, the long cycling of Li||LTE||Cu cells exhibit high stability with 95.5% CE$_{avg}$ during 100 cycle at 1 mA cm^{-2} and 25 °C, and 93.5% CE$_{avg}$ during 100 cycle at 0.5 mA cm^{-2} and −30 °C (Figure S10). However, the CE$_{avg}$ of Li||Cu cells using RE dropped sharply after 12th cycle, and reached 25.5% after 35th cycle at 25 °C (Figure 2d). The main reason is that the nucleation voltage in Li||RE||Cu cell was observed to be about 100.2 mV, which is higher than that of LTE (72.9 mV) (Figure 2e). Scanning electron microscopy (SEM) was used to visualize the morphology of lithium deposition on the Cu foil. Under the same plating capacity of 10 mAh, Figure 2f reveals the smooth and compact deposit morphologies of Li metal in LTE electrolyte. By contrast, a large amount of deposited Li particles featured with loose stacking and irregular morphology were observed for RE electrolytes (Figure 2g). The cross-sectional SEM images indicate that the deposition thickness of lithium metal in LTE and RE electrolytes is 40.4 and 58.3 μm (Figure 2h and Figure S11), respectively, implying that LTE electrolyte favors the uniformity and dense deposition of metal lithium.[35,36]

To demonstrate the electrochemical performance of the electrolyte, Li||NCM811 coin cells with different electrolytes were assembled and evaluated at different rates (Figure 3a).

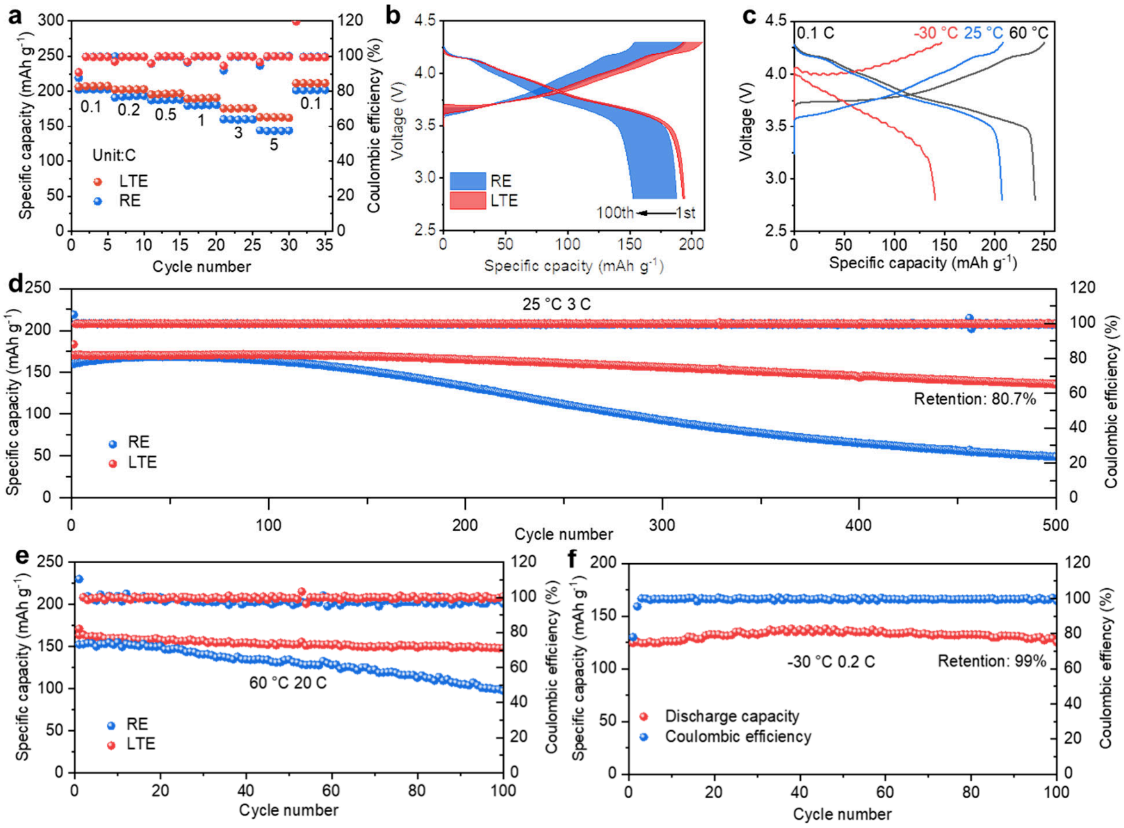

Figure 3. (a) Rate performance of Li||LTE||NCM811 and Li||RE||NCM811 at 25 °C. (b) Charge−discharge voltage profiles of Li||NCM811 cells using different electrolytes at 0.5 C and 25 °C. (c) Cycling performance of Li||LTE||NCM811 and Li||RE||NCM811 at 25 °C and a 3 C rate. (d) Charge−discharge voltage profiles of Li||LTE||NCM811 cells at different temperature. (e) Cycling performance of Li||LTE||NCM811 and Li||RE||NCM811 at 60 °C and 20 C rate. (f) Cycling performance of Li||LTE||NCM811 cells at −30 °C and 0.2 C rate.

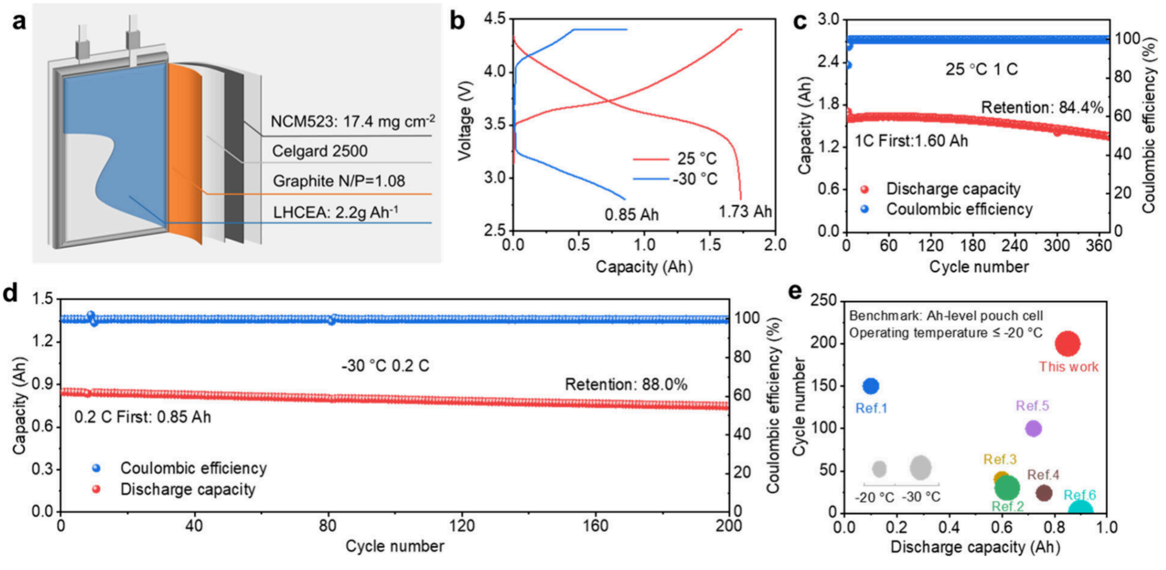

Figure 4. (a) Schematic diagram of Ah-level pouch cell. (b) Charge−discharge voltage profiles of Graphite||LTE||NCM523 pouch cells at different temperature. (c) Cycling performance of Graphite||LTE||NCM523 at 25 °C and 1 C. (d) Cycling performance of Graphite||LTE||NCM523 at −30 °C and 0.2 C. (e) The state-of-the-art performance of Ah-level pouch cells with extremely operating conditions in the published literature and this work.

The Li||LTE||NCM811 cells deliver discharge capacities of 207.5, 202.8, 196.6, 190.5, 176.2, and 163.1 mAh g^{-1} at 0.1, 0.5, 1, 2, 3, and 5 C, respectively. When the rate returns to 0.1 C, the cell still delivers a high capacity of 211.6 mAh g^{-1}. Figure 3b shows the charge−discharge voltage profiles of the Li||NCM811 cell employing RE and LTE at 0.5 C, and the capacity retention of the Li||LTE||NCM811 coin cell after 100 cycles is 99.4% (Figure S12). However, the polarization voltage of Li||RE||NCM811 cells reveal an increasing tendency along with the continuation of charging and discharging, the cells

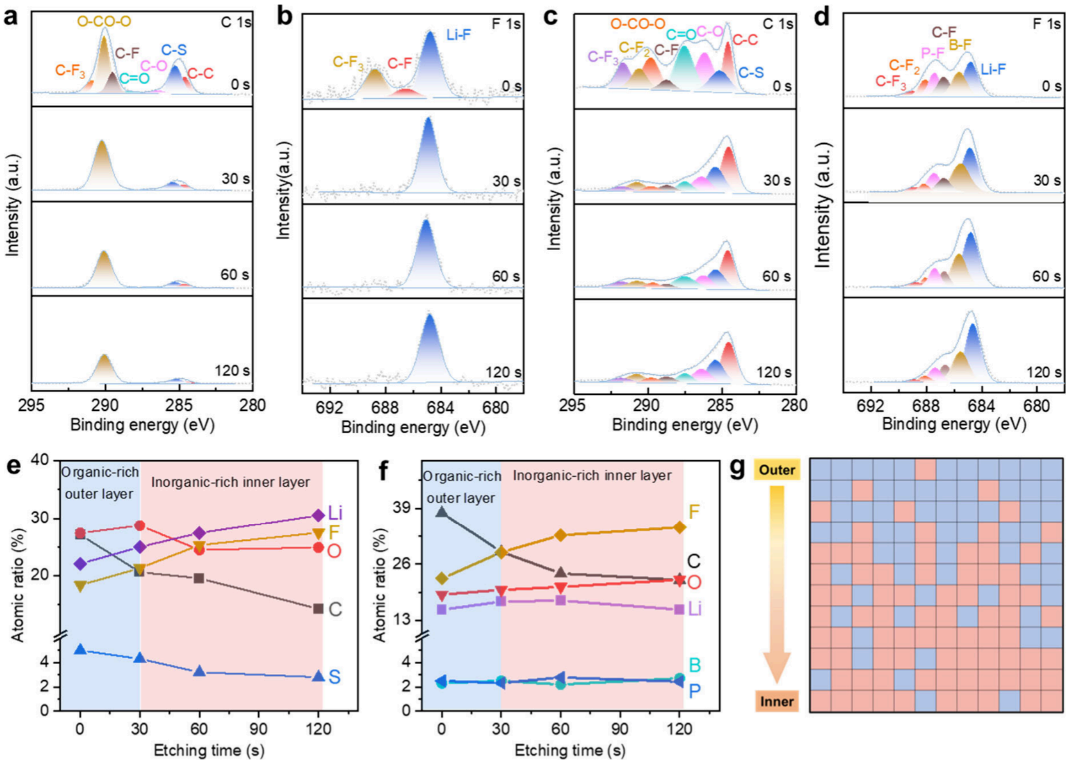

Figure 5. (a) C 1s spectra with depth profiles of the SEI formed in LTE electrolyte. (b) F 1s spectra with depth profiles of the SEI formed in LTE electrolyte. (c) C 1s spectra with depth profiles of the CEI formed in LTE electrolyte. (d) F 1s spectra with depth profiles of the CEI formed in LTE electrolyte. (e) Atomic ratio at different depths of the SEI formed in LTE electrolyte. (f) Atomic ratio at different depths of the CEI formed in LTE electrolyte. (g) The mosaic model of the interface layers formed in LTE electrolyte; the red squares represent inorganic composition, while blue squares represent organic composition.

finally maintain a lower retention of 81.5%. Figure 3d shows that the cycling performance of Li||NCM811 cells with LTE and RE, the Li||LTE||NCM811 cells exhibit a capacity retention of 80% after 500 cycles with an average CE of 99.9%. At a wide temperature range, the cells employing LTE show a high capacity of 240.5 mAh g^{-1} at 60 °C and 140.9 mAh g^{-1} at −30 °C (Figure 3c). Meanwhile, the Li||LTE|| NCM811 coin cells exhibit good cycling stability with retention of 90.9% at 60 and 20 C (Figure 3e) and 99% at −30 °C and 0.2 C (Figure 3f). In contrast, the Li||RE|| NCM811 cells show a severe capacity decay (63.8%) at high temperature and are unable to work at −30 °C due to electrolyte solidification (Figure S13).

To evaluate the practicality of the LTE electrolyte, the 1.8 Ah-class Li||NCM523 pouch cells were assembled for testing under different temperature conditions (Figure S14), the details of the pouch cells are shown in Figure 4a. The Li||LTE|| NCM523 pouch cells deliver a high capacity of 1.73 Ah at 0.2 C and 1.608 Ah at 1 C and 25 °C. After cycling for 375 cycles, the capacity retention of the pouch cell is 84.43% (Figure 4c). More significantly, the Li||NCM523 pouch cells with LTE are capable of charging and discharging at low temperatures, delivering a discharge capacity of 0.85 Ah at 0.2 C and −30 °C (Figure 4b). after 200 cycles, the pouch cell still maintains a high capacity retention of 88.3% with an average CE of 99.8% (Figure 4d), the results demonstrated that the capacity and retention of Li||NCM523 pouch cell with LTE are superior to that of low-temperature batteries reported in the literature (Figure 4e, Table S2).

The interface layer stemming from the electrolyte component is also crucial for low-temperature cycling stability of LIBs. The NCM811 cathode peeled off from cycled Li||RE|| NCM811 presents a 4.8 nm nonuniform CEI layer (Figure S15a). In contrast, the thickness of CEI from LTE is only 1.2 nm, which is uniformly distributed on the cathode surface (Figure S15 b). Figure S16a shows the XRD patterns of initial NCM811, cycled NCM811 with LTE and RE electrolytes, and the intensity ratios of (003)/(104) are 2.18, 1.96, and 1.2, respectively. Indicating the cycled NCM811 cathode with LTE has lower degree of Li$^+$/Ni^{2+} mixed than that of RE.[37] It is worth mentioning that the (003) peak of the cycled NCM811 cathode using LTE exhibits a slight shift about 0.04° (Figure S16b), which is smaller than that of the cycled NCM811 cathode using RE (0.16°). The results indicate that the CEI derived from LTE electrolyte can suppress harmful phase transitions.

In order to identify the interface chemistry well, X-ray photoelectron spectroscopy (XPS) was used to evaluate the composition of interface layers from cycled Li metal and NCM811 cathode. For the outer surface of CEI and SEI, the organic compositions mainly include O−CO−O, C═O, C−O, and C−F, which are generated from the decomposition of FEC and EMC solvents (Figure 5a and 5c). The inorganic composition mainly contains LiF, which is derived from the decomposition of anion-solvation structure (Figure 5b and d).[38] It is worth mentioning that the DTD decomposes into Li_xSO_y on the anodic surface (Figure S17a−c), while LiDFOB and $LiPO_2F_2$ decompose into LiF, B−F, and P−F on the cathodic surface (Figure S18a−c). When Ar$^+$ etching is applied, the organic signals (O−CO−O, C═O, C−O) that delivered from the decomposition of FEC and EMC solvents, present the significant decreasing trend after sputtering for 120 s (Figure 5e), while both B−F and LiF signals continuously strengthen throughout the sputtering process (Figure 5f), which agrees with the classic mosaic interface model (Figure 5g). The result indicates that the interface layers between electrodes and electrolyte have the obvious overlay layer features, where the layer approaching to the electrolyte mainly consists of organic composition, the layer close to the electrodes mainly contain inorganic composition.[39] As shown in Figure S19, the interface resistance of Li||LTE||NCM811 is 11.2, 24.3, and 49 Ω after 50th, 100th, and 200th cycles, which is much lower than that of Li||RE||NCM811, the results indicate the interface layers derived from the LTE have low Li^+ transport barrier and keep stable during the cycle. Benefiting from the superior SEI and CEI layers derived from LTE, the degree of side reaction is lower than that of using the RE electrolyte. After disassembling the cycled Li||LTE||NCM811 cells, the SEM images show that the surface of Li metal anode is smooth without metallic Li dendrites (Figure S20a, b), and the cathode particles remain intact without cracks (Figure S21a−d). In addition, in the pouch cell after full charge at −30 °C, the surface of the graphite anode is smooth without Li-dendrites and presents a golden yellow color (Figure S22), which indicates the Li-ions are completely inserted into the graphite anode, and there are no lithium dendrites during the entire process.

In summary, we have designed a carbonate-based electrolyte that achieves low-temperature and stable cycling LIBs through the combined effect of fluor-solvents and fluor-additives. The anion-solvation structure minimizes the Li^+-solvent binding energy, promoting rapid Li^+ desolvation. The DTD, LiDFOB, and $LiPO_2F_2$ participate in the construction of robust interface layers with inorganic components, reducing the interface transport energy barrier. Furthermore, the LTE extends the limits for low temperature LIBs with carbonate-based electrolyte, allowing Li||NCM811 cells to achieve 99% capacity retention at −30 °C after 100 cycles, and the practical graphite||NCM523 pouch cells enable high initial discharge capacity of 0.85 Ah at −30 °C, and 88% capacity retention after 200 cycles. Our findings provide guidance for the design of high-performance low temperature LIBs.

ASSOCIATED CONTENT

Supporting Information

The Supporting Information is available free of charge at https://pubs.acs.org/doi/10.1021/acsmaterialslett.5c00130.

> Experiment details, the physical properties of electrolyte, computational details, summary of the electrochemical performances, SEM images, XPS spectra, XRD pattern, and transmission electron microscopy images (PDF)

AUTHOR INFORMATION

Corresponding Authors

Baigang An − *School of Chemical Engineering, University of Science and Technology Liaoning, Anshan 114051, China;* orcid.org/0000-0001-6111-8166; Email: bgan@ustl.edu.cn

Chengguo Sun − *School of Chemical Engineering, University of Science and Technology Liaoning, Anshan 114051, China; School of Chemical Engineering Nanjing, University of Science and Technology, Nanjing 210094, China;* orcid.org/0000-0003-3580-2153; Email: sunyangguo2004@163.com

Authors

Hao Huang − *School of Chemical Engineering, University of Science and Technology Liaoning, Anshan 114051, China*

Yiyang Zhao − *School of Chemical Engineering, University of Science and Technology Liaoning, Anshan 114051, China*

Jingang Zheng − *School of Chemical Engineering, University of Science and Technology Liaoning, Anshan 114051, China*

Weichen Han − *School of Chemical Engineering, University of Science and Technology Liaoning, Anshan 114051, China*

Hongxu Zhou − *School of Chemical Engineering, University of Science and Technology Liaoning, Anshan 114051, China*

Hongyang Li − *School of Chemical Engineering, University of Science and Technology Liaoning, Anshan 114051, China*

Hongquan Chai − *School of Chemical Engineering, University of Science and Technology Liaoning, Anshan 114051, China*

Lixiang Li − *School of Chemical Engineering, University of Science and Technology Liaoning, Anshan 114051, China*

Hongwei Zhao − *School of Chemical Engineering, University of Science and Technology Liaoning, Anshan 114051, China*

Han Zhang − *School of Chemical Engineering, University of Science and Technology Liaoning, Anshan 114051, China;* orcid.org/0000-0001-6905-0952

Complete contact information is available at:
https://pubs.acs.org/10.1021/acsmaterialslett.5c00130

Author Contributions

Hao Huang: Data curation, Investigation, Methodology, Writing−original draft. **Yiyang Zhao:** Investigation, Methodology, Data curation. **Jingang Zheng:** Conceptualization, Methodology. **Weichen Han:** Software, Visualization. **Hongxu Zhou:** Methodology, Software. **Hongyang Li:** Methodology, Software. **Hongquan Chai:** Date curation, Software. **Lixiang Li:** Data curation, Visualization. **Hongwei Zhao:** Conceptualization, Resources. **Han Zhang:** Visualization, Software. **Baigang An:** Supervision, Funding acquisition, Writing-review and editing. **Chengguo Sun:** Funding acquisition, Project administration, Supervision, Writing-review and editing.

Notes

The authors declare no competing financial interest.

ACKNOWLEDGMENTS

This work was supported by the National Natural Science Foundation of China (11972178 and 52371224), the Nature Science Foundation of Liaoning Province (2023-BS-184). Distinguished Professor Project of Education Department of Liaoning and the Open Project Found of Key Laboratory of Energy Materials and Electrochemistry Liaoning Province are acknowledged.

REFERENCES

(1) Li, G.-X.; Jiang, H.; Kou, R.; Wang, D.; Nguyen, A.; Liao, M.; Shi, P.; Silver, A.; Wang, D. A superior carbonate electrolyte for stable cycling Li metal batteries using high Ni cathode. *ACS Energy Lett.* **2022**, *7*, 2282−2288.

(2) Lee, J.; Jeon, A.; Lee, H.; Shin, U.; Yoo, Y.; Lim, H.; Han, C.; Lee, C.; Kim, Y.; Baek, J.; Seo, D.; Lee, M. Molecularly engineered linear organic carbonates as practically viable nonflammable electrolytes for safe Li-ion batteries. *Energy Environ. Sci.* **2023**, *16*, 2924−2933.

(3) Deng, R.; Chu, F.; Kwofie, F.; Guan, Z.; Chen, J.; Wu, F. A Low-concentration electrolyte for high-voltage lithium-metal batteries: fluorinated solvation shell and low salt concentration effect. *Angew. Chem., Int. Ed.* **2022**, *61*, No. e202215866.

(4) Chen, Y.; He, Q.; Zhao, Y.; Zhou, W.; Xiao, P.; Gao, P.; Tavajohi, N.; Tu, J.; Li, B.; He, X.; et al. Breaking solvation dominance of ethylene carbonate via molecular charge engineering enables lower temperature battery. *Nat. Commun.* **2023**, *14*, 8326.

(5) Chen, L.; Wang, J.; Chen, M.; Pan, Z.; Ding, Y.; Song, Z.; Ai, X.; Cao, Y.; Chen, Z. "Dragging effect" induced fast desolvation kinetics and −50 °C workable high-safe lithium batteries. *Energy Storage Mater.* **2024**, *65*, No. 103098.

(6) Shadike, Z.; Chen, Y.; Liu, L.; Cai, X.; Shen, S.; Zhang, J. Improved cyclic stability of $LiNi_{0.8}Mn_{0.1}Co_{0.1}O_2$ cathode enabled by a novel CEI forming additive. *Front. Energy.* **2024**, *18*, 535−544.

(7) Liu, L.; Shadike, Z.; Wang, N.; Chen, Y.; Cai, X.; Hu, E.; Zhang, J. Low concentration electrolyte: A new approach for achieving high performance lithium batteries. *eScience* **2024**, *4*, No. 100268.

(8) Park, E.; Park, J.; Lee, K.; Zhao, Y.; Zhou, T.; Park, G.; Jeong, M.; Choi, M.; Yoo, D.; Jung, H.; et al. Exploiting the steric effect and low dielectric constant of 1,2 dimethoxypropane for 4.3 V lithium metal batteries. *ACS Energy Lett.* **2023**, *8*, 179−188.

(9) Piao, N.; Wang, J.; Gao, X.; Li, R.; Zhang, H.; Hu, G.; Sun, Z.; Fan, X.; Cheng, H.; Li, F. Designing temperature-insensitive solvated electrolytes for low temperature lithium metal batteries. *J. Am. Chem. Soc.* **2024**, *146*, 18281.

(10) Li, H.; Kang, Y.; Wei, W.; Yan, C.; Ma, X.; Chen, H.; Sang, Y.; Liu, H.; Wang, H. Branch-chain-rich diisopropyl ether with steric hindrance facilitates stable cycling of lithium batteries at −20 °C. *Nano-Micro Lett.* **2024**, *16*, 197.

(11) Lin, Y.; Yang, Z.; Zhang, X.; Liu, Y.; Hu, G.; Chen, S.; Zhang, Y. Activating ultra-low temperature Li-metal batteries by tetrahydrofuran-based localized saturated electrolyte. *Energy Storage Mater.* **2023**, *58*, 184−194.

(12) Li, G.; Koverga, V.; Nguyen, A.; Kou, R.; Ncube, M.; Jiang, H.; Wang, K.; Liao, M.; Guo, H.; Wang, J.; et al. Enhancing lithium-metal battery longevity through minimized coordinating diluent. *Nat. Energy.* **2024**, *9*, 817−827.

(13) Song, G.; Yi, Z.; Su, F.; Xie, L.; Wang, Z.; Wei, X.; Xu, G.; Chen, C. Boosting the low-temperature performance for Li-ion batteries in $LiPF_6$-based local high concentration electrolyte. *ACS Energy Lett.* **2023**, *8*, 1336−1343.

(14) Zhang, Q.; Zhang, X.; Hou, L.; Sun, S.; Zhan, Y.; Liang, J.; Zhang, F.; Feng, X.; Li, B.; Huang, J. Regulating solvation structure in nonflammable amide-based electrolytes for long-cycling and safe lithium metal batteries. *Adv. Energy Mater.* **2022**, *12*, No. 2200139.

(15) Xiao, P.; Zhao, Y.; Piao, Z.; Li, B.; Zhou, G.; Cheng, H. A nonflammable electrolyte for ultrahigh-voltage (4.8 V-class) Li|| NCM811 cells with a wide temperature range of 100 °C. *Energy Environ. Sci.* **2022**, *15*, 2435−2444.

(16) Zhang, A.; Bi, Z.; Wang, G.; Liao, S.; Das, P.; Lin, H.; Li, M.; Yu, Y.; Feng, X.; Bao, X.; et al. Regulating electrode/electrolyte interfacial chemistry enables 4.6 V ultra-stable fast charging of commercial $LiCoO_2$. *Energy Environ. Sci.* **2024**, *17*, 3021−3031.

(17) Wang, Y.; Zheng, H.; Hong, L.; Jiang, F.; Liu, Y.; Feng, X.; Zhou, R.; Sun, Y.; Xiang, H. Lithium difluoro(bisoxalato) phosphate-based multi-salt low concentration electrolytes for wide-temperature lithium metal batteries: experiments and theoretical calculations. *Chem. Eng. J.* **2022**, *445*, No. 136802.

(18) Wang, Z.; Zhang, H.; Xu, J.; Pan, A.; Zhang, F.; Wang, L.; Han, R.; Hu, J.; Liu, M.; Wu, X. Advanced ultralow-concentration electrolyte for wide-temperature and high voltage Li-metal batteries. *Adv. Funct. Mater.* **2022**, *32*, No. 2112598.

(19) Wang, Z.; Zhang, H.; Xu, J.; Pan, A.; Zhang, F.; Wang, L.; Han, R.; Hu, J.; Liu, M.; Wu, X. Advanced ultralow-concentration electrolyte for wide-temperature and high voltage Li-metal batteries. *Adv. Funct. Mater.* **2022**, *32*, No. 2112598.

(20) Xu, J.; Zhang, J.; Pollard, T.; Li, Q.; Tan, S.; Hou, S.; Wang, H.; Chen, F.; He, H.; Hu, E.; et al. Electrolyte design for Li-ion batteries under extreme operating conditions. *Nature* **2023**, *614*, 694−700.

(21) Meng, Y.; Zhou, D.; Liu, R.; Tian, Y.; Gao, Y.; Wang, Y.; Sun, B.; Kang, F.; Armand, M.; Li, B.; et al. Designing phosphazene-derivative electrolyte matrices to enable high-voltage lithium metal batteries for extreme working conditions. *Nat. Energy* **2023**, *8*, 1023−1033.

(22) Zhang, G.; Chang, J.; Wang, L.; Li, J.; Wang, C.; Wang, R.; Shi, G.; Yu, K.; Huang, W.; Zheng, H.; et al. A monofluoride ether-based electrolyte solution for fast-charging and low-temperature non-aqueous lithium metal batteries. *Nat. Commun.* **2023**, *14*, 1081.

(23) Lei, S.; Zeng, Z.; Yan, H.; Qin, M.; Liu, M.; Wu, Y.; Zhang, H.; Cheng, S.; Xie, J. Nonpolar cosolvent driving LUMO energy evolution of methyl acetate electrolyte to afford lithium-ion batteries operating at −60 °C. *Adv. Funct. Mater.* **2023**, *33*, No. 2301028.

(24) Li, Z.; Yao, Y.-X.; Zheng, M.; Sun, S.; Yang, Y.; Xiao, Y.; Xu, L.; Jin, C.-B.; Yue, X.-Y.; Song, T.; et al. Electrolyte design enables rechargeable $LiFePO_4$/graphite batteries from −80 to 80 °C. *Angew. Chem., Int. Ed.* **2025**, *12*, No. e202409409.

(25) Rampal, N.; Weitzner, S. E.; Cho, S.; Orme, C. A.; Worsley, M. A.; Wan, L. F. Structural and transport properties of battery electrolytes at sub-zero temperatures. *Energy Storage Mater.* **2024**, *17*, 7691−7698.

(26) Sun, S.; Wang, K.; Hong, Z.; Zhi, M.; Zhang, K.; Xu, J. Electrolyte design for low-temperature li-metal batteries: challenges and prospects. *Nano-Micro Letters.* **2024**, *16*, 35.

(27) Xu, J.; Koverga, V.; Phan, A.; Li, A.; Zhang, N.; Baek, M.; Jayawardana, C.; Lucht, B.; Ngo, A.; Wang, C. Revealing the anion-solvent interaction for ultralow temperature lithium metal batteries. *Adv. Mater.* **2024**, *36*, No. 2306462.

(28) Qin, K.; Li, S.; Yen, D.; Zhang, W.; Yang, Z.; Kamphaus, E.; Kim, E.; Huang, J.; Shea, J.; Hu, E.; et al. A coordinated-anion-enriched electrolyte for lean-electrolyte Li-S batteries. *ACS Energy Lett.* **2024**, *9*, 3869−3876.

(29) Wang, J.; Xie, L.; Wu, W.; Liang, Y.; Cao, M.; Gao, C.; Bo, Y.; Zhang, J.; Zhang, J. Boosting ultra-fast charging in lithium metal batteries through enhanced solvent−anion interaction via conjugation effect. *Energy Environ. Sci.* **2024**, *17*, 9100−9111.

(30) Ding, J.; Xu, R.; Yao, N.; Chen, X.; Xiao, Y.; Yao, Y.; Yan, C.; Xie, J.; Huang, J. Non-solvating and low-dielectricity cosolvent for anion-derived solid electrolyte interphases in lithium metal batteries. *Angew. Chem., Int. Ed.* **2021**, *60*, 11442−11447.

(31) Miao, X.; Hong, J.; Huang, S.; Huang, C.; Liu, Y.; Liu, M.; Zhang, Q.; Jin, H. In situ gel polymer electrolyte with rapid Li^+ transport channels and anchored anion sites for high-current-density lithium-ion batteries. *Adv. Funct. Mater.* **2025**, *35*, No. 2411751.

(32) Sun, M.; Xie, Y.; Zhong, C.; Huang, Y.; Chen, H.; Huang, H.; Dai, P.; Liu, S.; Zheng, W.; Liu, C.; et al. Bianionic coordination solvation structure electrolyte for high-voltage lithium metal batteries. *Energy Storage Mater.* **2024**, *65*, No. 103166.

(33) Ma, B.; Zhang, H.; Li, R.; Zhang, S.; Chen, L.; Zhou, T.; Wang, J.; Zhang, R.; Ding, S.; Xiao, X.; et al. Molecular-docking electrolytes enable high-voltage lithium battery chemistries. *Nat. Chem.* **2024**, *16*, 1427−1435.

(34) Wang, Y.; Yang, H.; Xu, j.; Tang, P.; Wei, Q.; Hu, T.; Gao, X.; Guo, Z.; Fang, R.; Hu, G.; et al. Competitive coordination of sodium ions for high-voltage sodium metal batteries with fast reaction speed. *J. Am. Chem. Soc.* **2024**, *146*, 7332−7340.

(35) Zhao, Y.; Zhou, T.; Mensi, M.; Choi, J.; Coskun, A. Electrolyte engineering via ether solvent fluorination for developing stable non-aqueous lithium metal batteries. *Nat. Commun.* **2023**, *14*, 299.

(36) Zhao, Y.; Zhou, T.; Baster, D.; El Kazzi, M.; Choi, J. W.; Coskun, A. Targeted functionalization of cyclic ether solvents for controlled reactivity in high-voltage lithium metal batteries. *ACS Energy Lett.* **2023**, *8*, 3180−3187.

(37) Zou, F.; Kim, J.; Zhang, J.; Lee, G.; Lyu, L.; Choi, J.; Kankaanpaeae, T.; Lee, Y.; Kang, Y. Optimal facet assembly of multi-transition metal layered cathodes toward superior Li-ion kinetics and structural stability. *Energy Environ. Sci.* **2024**, *17*, 4319−4326.

(38) Yao, N.; Sun, S.; Chen, X.; Zhang, X.; Shen, X.; Fu, Z.; Zhang, R.; Zhang, Q. The anionic chemistry in regulating the reductive stability of electrolytes for lithium metal batteries. *Angew. Chem., Int. Ed.* **2022**, *61*, No. e202210859.

(39) Zhang, J.; Zhang, H.; Weng, S.; Li, R.; Lu, D.; Deng, T.; Zhang, S.; Lv, L.; Qi, J.; Xiao, X.; et al. Multifunctional solvent molecule design enables high-voltage Li-ion batteries. *Nat. Commun.* **2023**, *14*, 2211.